Rare Metal Materials and Engineering
Volume 50, Issue 12, December 2021
Available online at www.rmme.ac.cn

Science Press

Cite this article as: Liu Anjin, Wang Lin, Cheng Xingwang, et al. Characterization of Hot Deformation Behavior and Processing Map of Powder Metallurgical High-Tungsten Steel[J]. Rare Metal Materials and Engineering, 2021, 50(12): 4201-4208.

ARTICLE

Characterization of Hot Deformation Behavior and Processing Map of Powder Metallurgical High-Tungsten Steel

Liu Anjin[1,2], Wang Lin[1,2], Cheng Xingwang[1,2], Xiong Zhiping[1,2], Ning Zixuan[1,2]

[1] School of Materials Science and Engineering, Beijing Institute of Technology, Beijing 100081, China; [2] National Key Laboratory of Science and Technology on Materials under Shock and Impact, Beijing Institute of Technology, Beijing 100081, China

Abstract: Hot deformation behavior of powder metallurgical high tungsten alloy steel was investigated by Gleeble thermal simulator in a temperature range of 900~1100 °C and a strain rate range of 0.001~1 s^{-1}. The results show that the flow stress decreases with the decrease of strain rate and the increase of deformation temperature. A constitutive equation is derived with Arrhenius hyperbolic sine function, and a processing map is constructed. The activation energy is 377 kJ/mol. The suitable processing regions are 1000~1100 °C/ 0.001~0.01 s^{-1}. The precipitation of tungsten-rich μ phase occurs during hot deformation process. Microvoids and micro-cracks form in the bulging region of the specimen. The amount of microvoid increases with the increase of strain rate and the decrease of temperature. The μ phase precipitation improves the high temperature strength of the steel.

Key words: tungsten steel; hot deformation behavior; constitutive model; processing map; microstructure

High-density alloys have been widely applied in the industrial, aerospace, and defense fields such as balance weight and kinetic energy projectile[1-3]. Nowadays, tungsten alloy is the mainly used high density alloy, which is based on tungsten with the addition of nickel and iron elements. Due to the existence of a large amount of tungsten element, powder metallurgy and liquid phase sintering (LPS) are commonly used methods to prepare tungsten alloy[4]. The strength of as-sintered tungsten alloy is usually below 1000 MPa. After severe plastic deformation, the strength of tungsten alloy can be improved to 1400 MPa, but the ductility will decrease significantly[5]. Compared with tungsten alloy, traditional steel exhibits a good matching of strength and plasticity, whereas the density is much lower than that of tungsten alloy. Tungsten (W) and molybdenum (Mo) are refractory elements with high density. The addition of W and Mo is the main method to improve the density of alloy. Powder metallurgy (P/M) is the preferred process for preparing high density alloy due to the advantages of high utilization of raw materials, simple process, uniform composition, and microstructure[6,7]. A novel high-density steel, based on the high strength steel and fabricated by P/M method, was introduced in this study in order to meet the industrial demand of high strength and density.

Although the P/M process has a series of advantages, it is generally considered that the subsequent high temperature deformation process is necessary to further improve the microstructure and mechanical properties of alloys. Processing map theory, developed by Prasad based on the dynamic material model (DMM) theory[8], has been widely applied in the thermal processing field as a promising method to study the deformation mechanism and to optimize the process parameters of steels[9-11], Ni-based superalloys[12], aluminum alloys[13] and titanium alloys[14,15]. DMM is a continuum model, in which an instability criterion based on extremum principles of irreversible thermodynamic is applied to a large flow described by Ziegler[16]. The power dissipation and the instability maps are plotted based on the temperature and strain, which can correlate processing regions with processing parameters. Lu et al[17] conducted hot compression on spray-formed high-speed steel, indicating that a small range of temperature (1050~1150 °C) and strain rate (0.01~ 0.1 s^{-1}) can be used as a safe domain for hot compression. Wang et al[18] investigated the hot deformation behavior of powder sintered multi-crystalline tungsten in a temperature range of 1250~1550 °C and a strain rate range of 0.001~1 s^{-1},

Received date: December 20, 2020
Corresponding author: Wang Lin, Ph. D., Associate Professor, School of Materials Science and Engineering, Beijing Institute of Technology, Beijing 100081, P. R. China, E-mail: linwang@bit.edu.cn

established the processing map at a strain of 0.1~0.6, and showed that dynamic recovery (DRV) is the principal softening effect at elevated temperatures. Mirzadeh et al[19] studied the dynamic recrystallization (DRX) and DRV through stress-strain curves of medium carbon microalloyed steel and calculated activation energy during hot deformation. Sun et al[20] established the processing map of powder metallurgy TiAl-based alloy at 950~1200 °C and 0.001~0.1 s^{-1} which showed the refined microstructure due to DRX. Tan et al[21] constructed the processing map of P/M fabricated superalloy and it showed less cracking risk in hot compression under 1000~1100 °C and 0.001~1 s^{-1}, indicating a promising potential to forge the P/M superalloys without grain refinement by hot extrusion. Although many studies have dealt with the hot deformation behavior of different alloys through processing maps, it is still difficult to use the existing process to predict the deformation behavior of novel high tungsten steel. The high content of the W element in the designed steel may result in brittleness during the hot deformation. Therefore, it is necessary to investigate the hot deformation behavior and microstructure evolution. This work studied the hot deformation behavior of novel steel and established the constitute equation and processing maps, hoping to optimize and guide the hot working process.

1 Experiment

1.1 Materials preparation

High-tungsten steel has been recently developed using powder metallurgy. Firstly, tungsten, molybdenum, and 18Ni maraging steel (18Ni8.5Co5Mo0.4Ti0.1Al, wt%) powders were mechanically mixed with a mass ratio of 22: 4: 74. Secondly, the mixed powders were milled in a planetary ball mill using a ball-to-powder mass ratio of 5: 1 for 12 h at a milling speed of 300 r/min. Thirdly, the milled powders were cold isostatically pressed (CIP) for 40 min at a pressure of 250 MPa. Finally, the sample was hot isostatically pressed (HIP) at 1300 °C and 130 MPa for 4 h in argon atmosphere. The microstructure of this high-tungsten steel, as shown in Fig. 1, has equiaxed grains with an average grain size of 80 μm. The density is 9.3 g/cm^3 measured by the Archimedean principle.

1.2 Hot compression tests

Hot compression tests were conducted on a Gleeble 3500 thermal simulator at different temperatures and strain rates under a vacuum of about 1 Pa. Cylindrical specimens with an aspect ratio of 1.5 (6 mm in diameter and 9 mm in length) were machined from HIPed alloys. A pair of highly sensitive thermocouples were welded at the mid-length of the specimen to measure and control the temperature during hot compression. The specimens were heated to 1200 °C at a rate of 10 °C/s, held for 3 min to eliminate temperature gradient, and then cooled at a rate of 5 °C/s to the deformation temperatures. The isothermal compression was conducted in the range of 900~1100 °C with intervals of 50 °C. The strain rate was set as 0.001, 0.01, 0.1, and 1 s^{-1}. The cylindrical specimens were deformed to a 40% reduction, and a tantalum sheet was placed between specimen and anvil to reduce the friction. Finally, the specimens were water quenched to room temperature. The flow stress was recorded as a function of strain for each compression test.

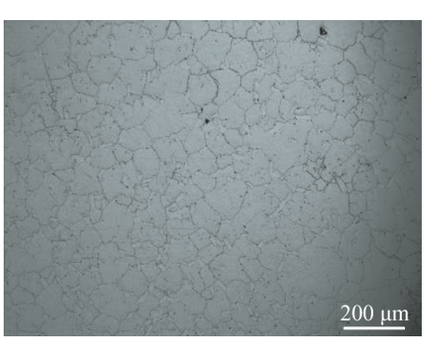

Fig.1 Optical microstructure of as-sintered high-tungsten steel

1.3 Microstructure observation

The deformed specimens were cut along the compression axis in the center and mounted in the resin for metallographic observation. The mounted specimens were ground and polished, followed by etching in 4% HNO_3 alcohol solution. The microstructures were characterized by optical microscope (OM, Zeiss ProgRes C5) and scanning electron microscope (SEM, FEI Quanta 650) equipped with energy backscatter diffraction (EBSD) detector. The crystalline structure was identified by X-ray diffraction (XRD) using Bruker D8 diffractometer with Co Kα radiation operated at 35 kV/40 mA with a scanning range from 30° to 100° . The foils for transmission electron microscopy (TEM) were prepared by grinding to the thickness of 40 μm and thinning by the ion beam thinning method. The TEM observation was performed on JEM-2100 TEM with an acceleration voltage of 200 kV.

2 Results and Discussion

2.1 Analysis of flow stress curves

The true stress-true strain curves during isothermal compression are shown in Fig. 2. The flow curves correspond to the deformation temperatures of 900, 950, 1000, 1050, and 1100 °C at different strain rates of 0.001, 0.01, 0.1, and 1 s^{-1}. The flow stress curves are sensitively dependent on the temperature and strain rate. At the incipient deformation stage, flow stress increases significantly with increasing the strain rate and decreasing the temperature. During deformation, the flow stress increases sharply to the peak stress at the beginning of deformation followed by slight declination. The flow stress shows a continuous strain softening at the strain rate lower than 0.1 s^{-1} at each deformation temperature. In contrast, at a strain rate of 1 s^{-1}, these curves exhibit a relatively steady state.

At the initial stage of deformation, the work hardening effect is the dominant reason for the increase of flow stress. The propagation and accumulation of dislocation occur with an increase in deformation strain, leading to an increase in strain hardening effect. Meanwhile, the thermal activation

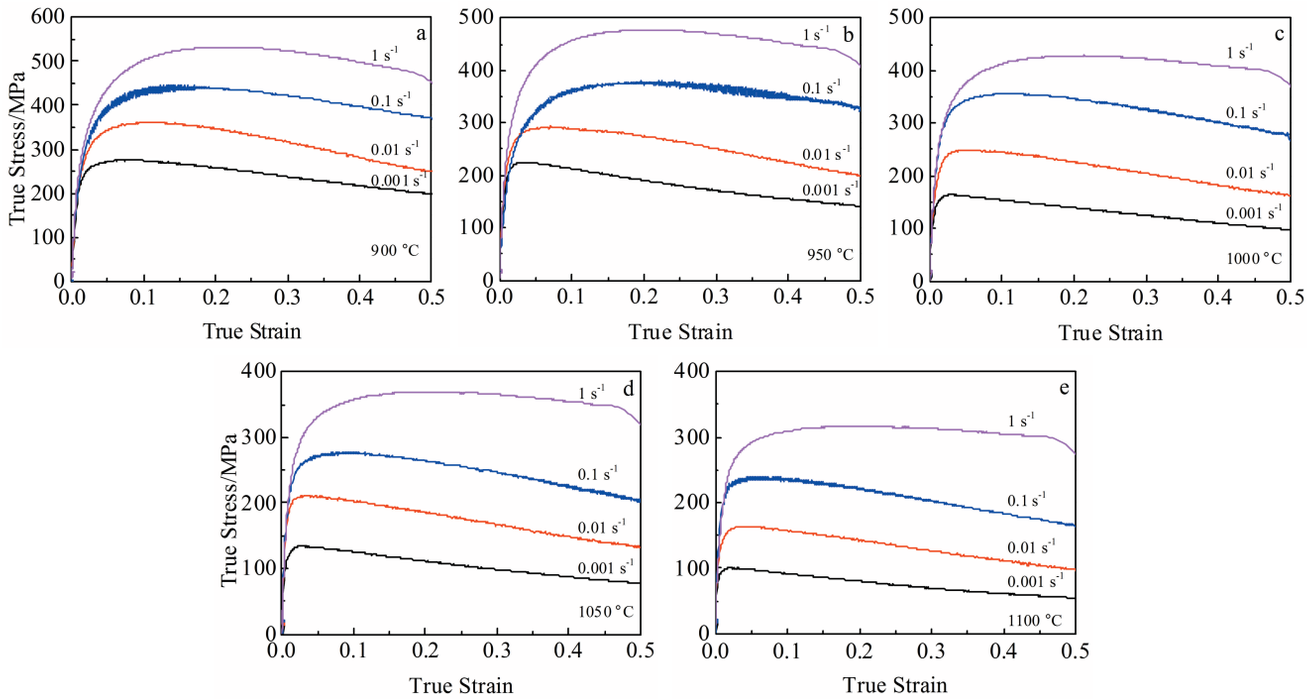

Fig.2 True stress-strain curves of the high-tungsten alloy at different strain rates and different deformation temperatures: (a) 900 °C, (b) 950 °C, (c) 1000 °C, (d) 1050 °C, and (e) 1100 °C

promotes the nucleation and growth of sub-grains. Thus, dynamic recovery also occurs at the same time as strain hardening. With increasing the deformation temperature, dynamic recovery develops faster, and it takes less time to reach the peak stress[22]. The flow curves at low strain rates show an apparent softening phenomenon after the peak stress, indicating that the dynamic recovery offsets the work hardening effect. It is probably that the accumulated dislocations in the deformation process result in the nucleation core of dynamic recrystallization. Furthermore, the dislocations are eliminated during the process of grain growth of dynamic recrystallization. As a result, the stress-strain curves exhibit a decreasing trend for the softening effect.

2.2 Establishment of the constitutive relationship

The flow stress evolution at high deformation temperature is related to the strain rate ($\dot{\varepsilon}$), deformation degree (ε), and temperature (T). The relationship between flow stress, strain rate, and deformation temperature is generally described in the form of Arrhenius equation, as follows:

$$\dot{\varepsilon} = A\sigma^n \exp\left(-\frac{Q}{RT}\right) = A\left[\sinh(\alpha\sigma)\right]^n \exp\left(-\frac{Q}{RT}\right) \quad (1)$$

$$\dot{\varepsilon} = A_1\sigma^{n_1} \exp\left(-\frac{Q}{RT}\right) \quad (2)$$

$$\dot{\varepsilon} = A_2 \exp(\beta\sigma)\exp\left(-\frac{Q}{RT}\right) \quad (3)$$

where Q (kJ/mol) is the activation energy of deformation, R is the gas constant (8.314 J/(mol·K)), A_1, A_2, A, n_1, n, β and α ($\approx\beta/n_1$) are material constants determined by deformation, and σ is the flow stress. Eq. (2) and Eq. (3) are suitable for low stress and high stress conditions, respectively, while Eq. (1) can be used in a wide range of temperatures and strain rates[23].

The effects of temperature and strain rate under hot working process on deformation behavior can be analyzed using the hyperbolic sine function incorporated in the Zener-Hollomon parameter (Z). It can be expressed as follows:

$$Z = \dot{\varepsilon}\exp\left(\frac{Q}{RT}\right) = A\left[\sinh(\alpha\sigma)\right]^n \quad (4)$$

The values of n_1 and β can be calculated by linear regression of equations obtained by taking logarithm on each side of Eq. (2) and Eq. (3), which are shown in Fig. 3a and Fig. 3b. The average values of n_1 and β are calculated as 7.9719 and 0.028 27, respectively. Then Eq. (5) can be obtained by taking a natural logarithm from each side of Eq.(4) and rewritten as Eq.(6).

The plots of the linear regression relationship between $\ln[\sinh(\alpha\sigma)]$ and $\ln\dot{\varepsilon}$ are shown in Fig.3c, which can determine the value of stress exponent, n. The plot of $\ln[\sinh(\alpha\sigma)]$ and $1/T$ is used for calculating the value of activation energy Q, as shown in Fig.3d.

$$\ln\dot{\varepsilon} + \frac{Q}{RT} = \ln A + n\ln\left[\sinh(\alpha\sigma)\right] \quad (5)$$

$$\ln\sinh(\alpha\sigma) = \left(\frac{\ln\dot{\varepsilon} - \ln A}{n}\right) + \frac{Q}{nRT} \quad (6)$$

From Eq.(6), the stress exponent n can be calculated as:

$$n = \left[\frac{\partial\ln\dot{\varepsilon}}{\partial\ln\sinh(\alpha\sigma)}\right]_T \quad (7)$$

The values of α and n were determined as 0.003 546 and 5.8525, respectively. The activation energy for isothermal deformation at a constant strain rate is determined by Eq. (8)

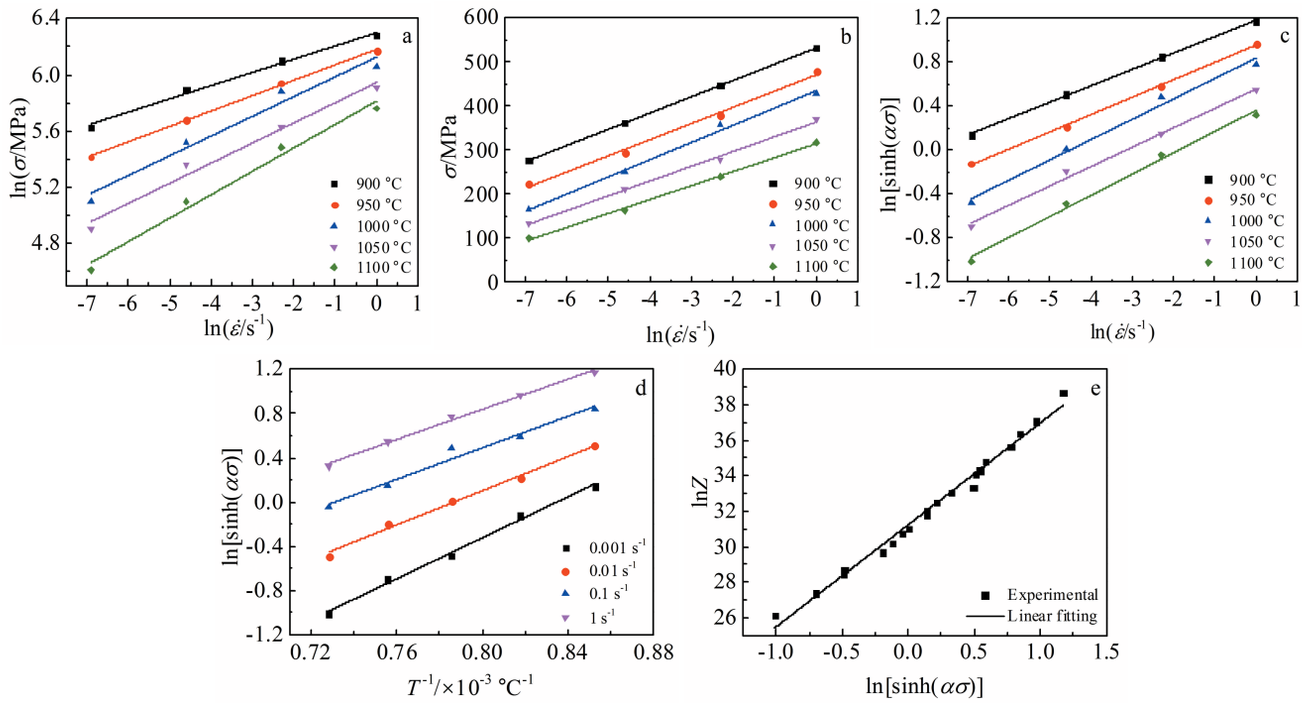

Fig.3 Relationships among various parameters of studied steel under different hot deformation conditions: (a) lnσ-ln$\dot{\varepsilon}$, (b) σ-ln$\dot{\varepsilon}$, (c) ln[sinh($\alpha\sigma$)]-ln$\dot{\varepsilon}$, (d) ln[sinh($\alpha\sigma$)]-1/T, and (e) ln$Z$-ln[sinh($\alpha\sigma$)]

as follows:

$$Q = Rn\left[\frac{\partial \ln \sinh(\alpha\sigma)}{\partial(1/T)}\right]_{\dot{\varepsilon}} \tag{8}$$

The average activation energy is 377 kJ/mol which is calculated by the sinh type equation. By substituting the values α, n, Q and A into Eq. (4), the constitutive equation is obtained for powder metallurgy high-tungsten steel using sinh type law in the temperature range of 900~1100 °C and the strain rate range of 0.001~1 s^{-1}, as shown in Eq.(9).

$$Z = \dot{\varepsilon}\exp\left(\frac{377\,000}{RT}\right) = 3.6618 \times 10^{13}[\sinh(0.003\,546\sigma)]^{5.8525} \tag{9}$$

Fig. 3e shows the variation of the Zener-Hollomon parameter as a function of peak flow stress, and relationship of ln$Z$ versus ln[sinh($\alpha\sigma$)] is listed in Eq.(10). The peak flow stress obtained from different hot deformation conditions is fitted well with the Zener-Hollomon parameter, showing a good linear correlation of the regression coefficient (R^2=0.98).

$$\ln Z = 5.7541\ln[\sinh(\alpha\sigma)] + 31.231 \tag{10}$$

The Q value of powder metallurgy high-tungsten alloy is determined to be 377 kJ/mol, which is higher than 355 kJ/mol of 18Ni maraging steel[24]. However, this Q value of the studied alloy is similar to that of the 18Ni maraging steel because the studied alloy is made of 74 wt% 18Ni steel. The studied alloy is sintered by CIP and HIP methods, and the tungsten is a refractory element with a high melting temperature. According to the Fe-W phase diagram[25], the maximum solid solubility for tungsten in Fe is 32.5% at 1540 °C, while it decreases to 4.5% at 700 °C. Besides, the atom diffusion during the powder metallurgy process is not as fast as the smelting process. Therefore, the limited solid solubility of tungsten will not lead to significant increase in the activation energy of this powder metallurgy alloy.

2.3 Characterization of processing map and microstructural evolution

For the powder metallurgy alloy, it is easy to induce microvoids, cracks, and even macro damage during deformation. The mechanical behavior of alloys is related to the flow stress (σ), strain rate ($\dot{\varepsilon}$), strain (ε), and temperature (T). Therefore the processing map, consisting of power dissipation map and instability map, can be a promising method to instruct the hot deformation process. According to the principle of DMM, the power (P) absorbed by the samples during hot deformation can be described using two complementary functions, G and J, as follows:

$$P = G + J = \sigma\dot{\varepsilon} = \int_0^{\dot{\varepsilon}} \sigma \mathrm{d}\dot{\varepsilon} + \int_0^{\sigma} \dot{\varepsilon}\mathrm{d}\sigma \tag{11}$$

where G represents the power dissipated during plastic deformation, mostly losing in the form of deformation heat, while the co-content J is related to the microstructural evolution.

The power partition between J and G can be expressed by Eq.(12), which is known as strain rate sensitivity parameter m:

$$\frac{\mathrm{d}J}{\mathrm{d}G} = \frac{\dot{\varepsilon}\mathrm{d}\sigma}{\sigma\mathrm{d}\dot{\varepsilon}} = \frac{\mathrm{d}(\ln\sigma)}{\mathrm{d}(\ln\dot{\varepsilon})} = m \tag{12}$$

where m is connected with σ and $\dot{\varepsilon}$:

$$\sigma = K\dot{\varepsilon}^m \tag{13}$$

From Eq. (11) and Eq, (12), at a given deformation temperature T and strain ε, the co-content J can be described as

$$J = \frac{m}{m+1}\sigma\dot{\varepsilon} \tag{14}$$

For an ideal linear dissipation process, m = 1; the value of J reaches its maximum, $J_{max}=\sigma\dot{\varepsilon}/2$. The efficiency of the power dissipation η can be deduced by:

$$\eta = \frac{J}{J_{max}} = \frac{2m}{1+m} \tag{15}$$

Dharmendra[26] developed a continuum criterion based on extremum principles of irreversible thermodynamics, which can be expressed by a dimensionless parameter $\xi(\dot{\varepsilon})$, as shown in Eq.(16).

$$\xi(\dot{\varepsilon}) = \frac{\partial \ln\left(\frac{m}{m+1}\right)}{\partial \ln \dot{\varepsilon}} + m < 0 \tag{16}$$

The value of instability parameter $\xi(\dot{\varepsilon})$ becomes negative when the specimen is in the region of flow instability. The cubic spline interpolation method was used to calculate the flow stress values at a finer interval of temperatures and strain rates, using the experimental data points obtained by the Gleeble test as knots. Therefore, the value of strain rate sensitivity, the efficiency of power dissipation, and the instability parameter can be calculated through the equations mentioned above.

Based on the data obtained in hot deformation experiments at different strain rates, temperatures, and strains, the processing maps of studied alloy are constructed by dissipation efficiency map and instability map at strains of 0.2, 0.3, 0.4, and 0.5, as shown in Fig.4. The contour numbers represent the power dissipation efficiency (η), and the shaded area represents the instable domain judged by instability parameter $\xi(\dot{\varepsilon})$. It shows a high-efficiency region at lower strain rates and higher temperatures. Besides, the power dissipation maps exhibit similar shape at strains ranging from 0.2 to 0.5. With increasing the strain, the region with a large value of dissipation efficiency becomes larger. In general, the value of η in the DRV domination region is about 0.3, while it is 0.3~0.5 in the DRX region[27]. The maximum efficiency is above 0.4 in the region of temperature above 1050 °C and strain rate below 0.01 s^{-1}. Meanwhile, it is noticeable that the peak power dissipation efficiency at the high strain rate area increases when the true strain increases. For example, an efficiency above 0.33 can be obtained at the deformation temperature above 1050 °C and strain rate up to 1 s^{-1} (Fig.4b and Fig.4c). However, this region is close to the unstable area and relatively narrow, and it is still not suitable for bulk metal processing. The instability maps at different true strains show that the unstable region becomes larger with increasing the strain. The unstable regions mainly locate at high strain rates (>0.1 s^{-1}) and low temperatures (<1025 °C). Thus, the suitable processing regions are 1000~1100 °C/0.001~0.01 s^{-1}, with an efficiency above 37%. For powder metallurgy alloys, wedge cracking, prior particle boundary, and shear bands may contribute to the flow instability.

Fig. 5 shows the optical microscope microstructure of the deformed power metallurgy high-tungsten steel. The deformed samples can be divided into four regions (as seen in Fig. 5a): (I) non-deformed region near both ends of specimen, (II) transition deformation region adjacent to the non-deformed region, (III) homogenous deformation region in the center of specimen, and are (IV) circum swelling deformation

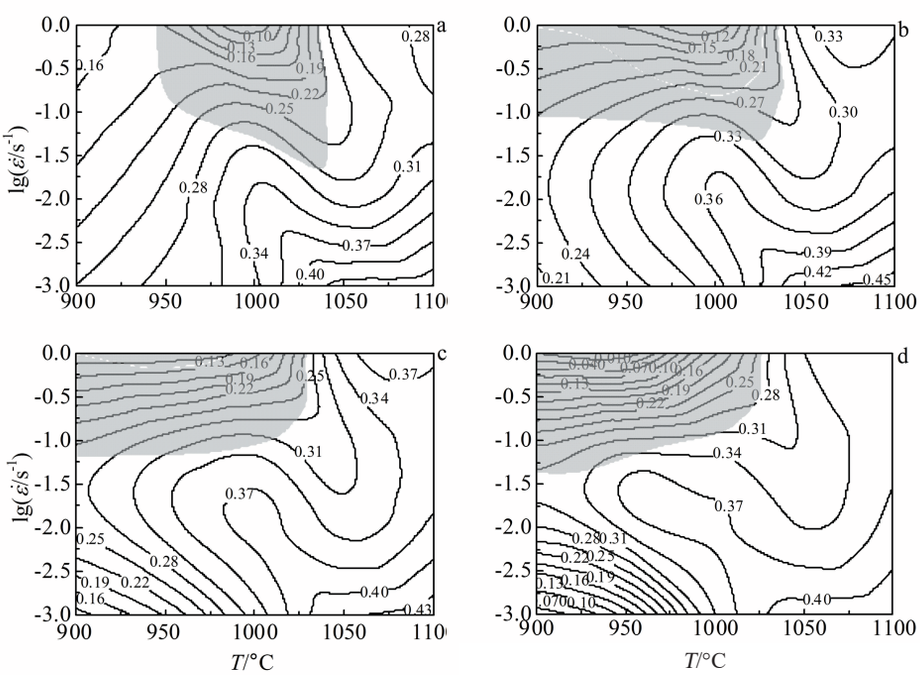

Fig.4 Processing maps established from hot compression data at strains of 0.2 (a), 0.3 (b), 0.4 (c) and 0.5 (d) (the contour numbers represent the efficiency of power dissipation, while the shaded area represents the instability area)

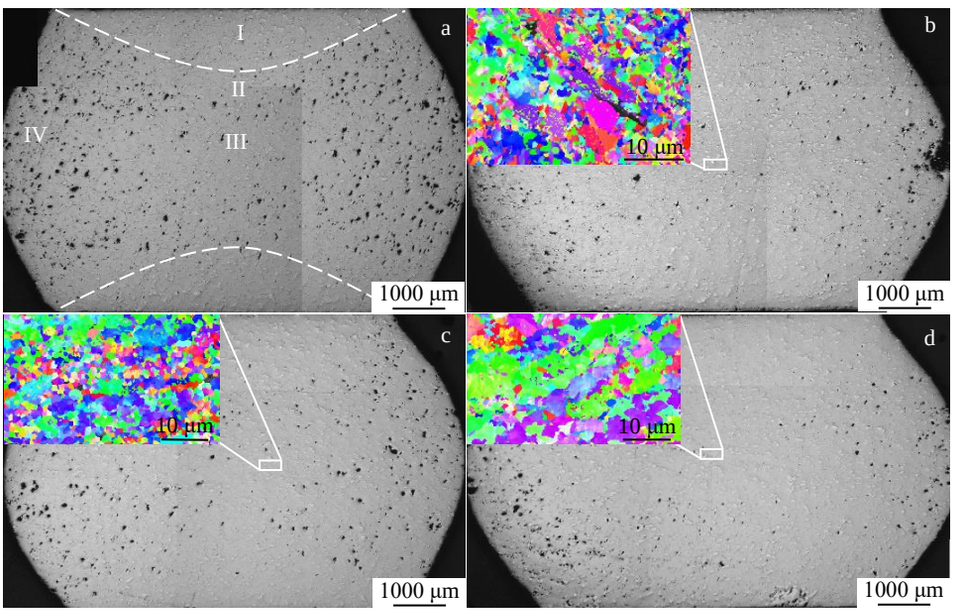

Fig.5 OM microstructures and EBSD images of the region along the compression axial at different temperatures and strain rates: (a) 950 °C/1 s^{-1}, (b) 1000 °C/0.001 s^{-1}, (c) 1100 °C/1 s^{-1}, and (d) 1100 °C/0.001 s^{-1}

region[28]. It is obvious that microvoids appear in the specimens and are mainly distributed in the circum swelling deformation region. With increasing the strain rate and decreasing the deformation temperature, the number of microvoids increases, which corresponds to the instability region in processing maps. The homogenous deformation region in the center of the specimen shows a better microstructure with few microvoids at high temperature and low strain rate, as shown in Fig. 5b and Fig. 5c. The EBSD images in insets of Fig. 5 illustrate the grain structure at the center region of the specimen after deformation. It can be confirmed that the grains are refined in the steel deformed at high strain rate, and the grain size is enlarged at low strain rate and high temperature. The average grain size of sample compressed at 1100 °C/1 s^{-1} is as large as 2 μm, and that is 3.8 μm at 1100 °C/0.001 s^{-1}. Compared with these two conditions, grain size deformed at 1000 °C/0.001 s^{-1}, shown in Fig. 5b, is slightly larger than that deformed at 1100 °C/1 s^{-1}. The higher temperature enhances the driving force for dislocation mobility and grain boundary migration and results in the coarsening of recrystallized grains[29].

The magnified images, focusing on the homogenous deformation region at different strain rates and temperatures, are shown in Fig. 6. White parts are the accumulation of tungsten, while the gray area represents the maraging steel as the matrix. Meanwhile, many fine particles precipitate in the matrix with an average size of 0.86 μm. Fig. 7a presents the XRD patterns of the as-received sample and those after deformation at different temperatures. The prominent peaks of as-received samples represent the fcc phase corresponding to the steel, and small peaks represent the μ phase. The μ phase has the topological close-packed (TCP) structure, which has a significant effect on the properties of the alloy[30]. With increasing deformation temperature, the intensity of fcc phase peaks decreases, and that of the μ phase increases, indicating that increasing deformation temperature can increase the amount of precipitation.

As shown in Fig. 6a, several micro-cracks appear in the tungsten enrichment area at low temperatures and high strain rates, which also corresponds to the unstable domain in the processing map. In Fig. 6b and Fig. 6c, no apparent defect is observed in the homogenous deformation region with increasing deformation temperature. The grains and precipitated particles in this region suffer severe deformation and fragmentation. Equiaxial grains are elongated along the direction vertical to the compression axial. A large amount of μ phase particles with tiny size precipitated during the deformation process can delay the nucleation of recrystallization. Meanwhile, the pinning effect of precipitated particles on grain boundaries may even inhibit the recrystallization, and the stored energy is hard to initiate DRX and grain growth. The grain size represented by EBSD images in Fig. 5 shows that even under high temperature and low strain rate deformation conditions, the grain size increases slightly, which is still smaller than the initial microstructure. Fig. 6d is the magnified SEM image of cracks in the circum region. Cracks are developed along the interface between tungsten enrichment region and μ phase particles and the steel matrix. The bulge of the cylinder surface causes tensile stress at circum direction. The μ phase, which has been identified through XRD and TEM (Fig. 7), has a complex rhombohedral lattice with A_7B_6 structure where A is occupied by transition metal and B is refractory metal, such as Fe_7W_6 and Co_7Mo_6[31]. Fig. 7c also shows the diffraction pattern taken from the white

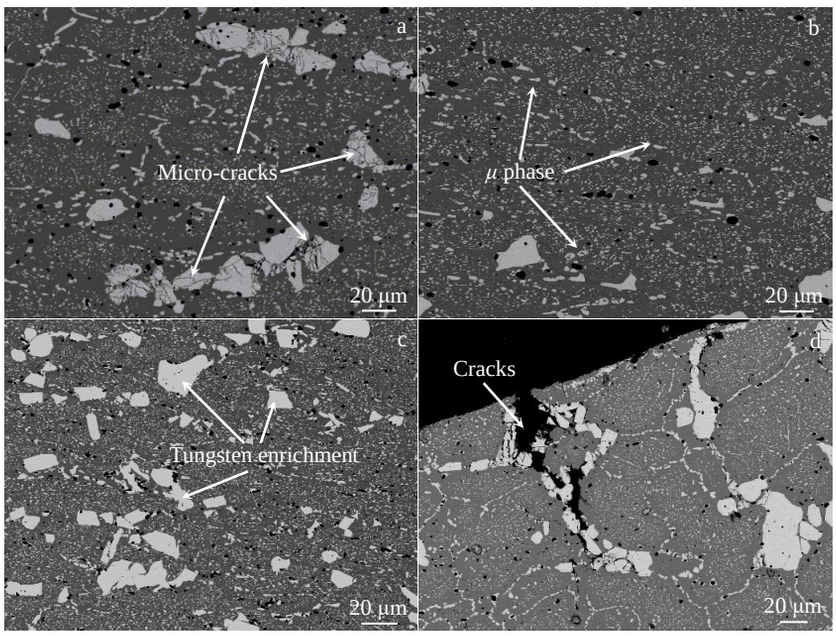

Fig.6 SEM images of the center region of deformed samples (a~c) and circum swelling region (d): (a) 1000 °C/1 s^{-1}, (b) 1100 °C/0.001 s^{-1}, and (c, d) 1100 °C/1 s^{-1}

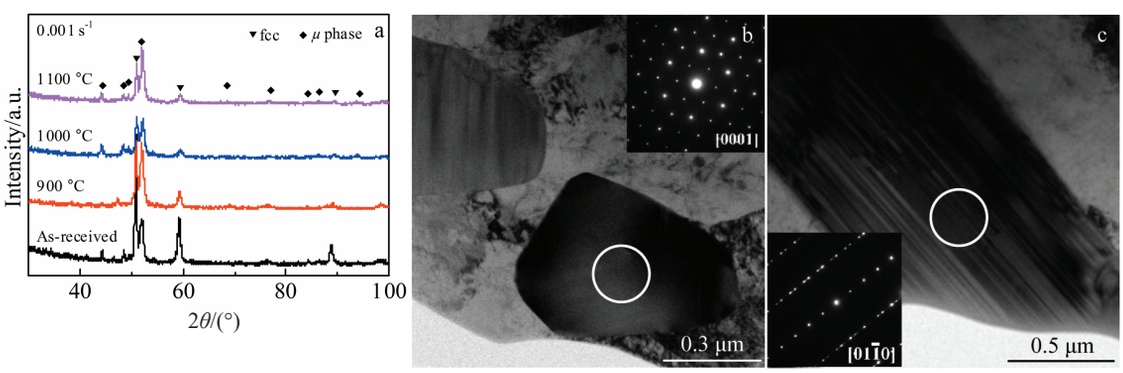

Fig.7 XRD patterns of samples deformed at different temperatures (a); bright-field TEM images of the μ phase in alloy with corresponding SAED patterns in the insets showing μ phase precipitation (b, c)

circle and it can be indexed as the [$01\bar{1}0$] zone axis with twinning structures. In addition, the precipitation of the μ phase during hot deformation can improve the strength of steel as the strengthened particles compared with the 18Ni maraging steel[32].

3 Conclusions

1) The flow stress of P/M high-tungsten steel increases with increasing the strain rate and decreasing the deformation temperature. The activation energy of the studied steel is 377 kJ/mol. The constitutive equation of the Zener-Hollomon parameter is successfully established, namely $Z = 3.6618 \times 10^{13}[\sinh(0.003\,546\sigma)]^{5.852\,5}$

2) The processing map is successfully established, indicating that the domain at the strain rate of 0.001~0.01 s^{-1} and temperature of 1000~1100 °C has an efficiency above 37%. It can be considered as an optimum hot working condition.

3) The area of instability domains in the processing map increases with increasing the strain. The processing map shows an instability domain that occurs at the temperature below 1000 °C and the strain rate above 0.1 s^{-1}. Moreover, this domain should be avoided in the hot working process.

4) The addition of tungsten and precipitation of the μ phase are the main sources of crack propagation during the hot deformation process.

References

1 Rao A S, Manda P, Mohan M K *et al. Journal of Alloys and*

Compounds[J], 2018, 742: 937
2 Ding L, Xiang D P, Li Y Y *et al. Materials & Design*[J], 2012, 37: 8
3 Kiran U R, Panchal A, Sankaranarayana M *et al. International Journal of Refractory Metals and Hard Materials*[J], 2013, 37: 1
4 Pathak A, Panchal A, Nandy T K *et al. International Journal of Refractory Metals & Hard Materials*[J], 2018, 75: 43
5 Wu Y C, Hou Q Q, Luo L M *et al. Journal of Alloys and Compounds*[J], 2019, 776: 926
6 Upadhyaya G S. *Powder Metallurgy Technology*[M]. Cambridge: Cambridge Int Science Publishing, 1997
7 Güral A, Tekeli S. *Materials & Design*[J], 2007, 28: 1224
8 Prasad Y, Gegel H. *Metallurgical and Materials Transactions A* [J], 1984, 15: 1883
9 Momeni A, Dehghani K. *Materials Science and Engineering A* [J], 2010, 527: 5467
10 Liu G W, Han Y, Shi Z Q *et al. Materials & Design*[J], 2014, 53: 662
11 Sun C Y, Li Y M, Xiang Y *et al*. *Rare Metal Materials and Engineering*[J], 2016, 45(3): 688 (in Chinese)
12 Wen D X, Lin Y C, Li H B *et al. Materials Science and Engineering A*[J], 2014, 591: 183
13 Wang Y X, Zhao G Q, Xu X *et al. Journal of Alloys and Compounds*[J], 2019, 779: 735
14 Zhu Y C, Zeng W D, Feng F *et al. Materials Science and Engineering A*[J], 2011, 528: 1757
15 Li C W, Xie H, Mao X N *et al*. *Rare Metal Materials and Engineering*[J], 2017, 46(2): 326
16 Rajput S K, Chaudhari G P, Nath S K. *Journal of Materials Processing Technology*[J], 2016, 237: 113
17 Lu L, Hou L G, Cui H *et al. Journal of Iron and Steel Research International*[J], 2016, 23(5): 501
18 Wang J, Zhao G, Li M. *Materials & Design*[J], 2016, 103: 268
19 Mirzadeh H, Cabrera J M, Prado J M *et al. Materials Science and Engineering A*[J], 2011, 528: 3876
20 Sun Y, Wan Z P, Hu L X *et al. Materials & Design*[J], 2015, 86: 922
21 Tan L M, Li Y P, He G A *et al. Materials Characterization*[J], 2019, 147: 340
22 Lin Y C, Li L T, Xia Y C *et al. Journal of Alloys and Compounds* [J], 2013, 550: 438
23 Mirzadeh H, Cabrera J M, Prado J M *et al. Materials Science and Engineering A*[J], 2011, 528: 3876
24 Avadhani G S. *Journal of Materials Engineering & Performance* [J], 2003, 12: 609
25 Jacob A, Schmetterer C, Singheiser L *et al. Calphad: Computer Coupling of Phase Diagrams & Thermochemistry*[J], 2015, 50: 92
26 Dharmendra C, Rao K P, Jain M K *et al. Journal of Alloys and Compounds*[J], 2018, 744: 289
27 Liu Y H, Ning Y Q, Yao Z K *et al. Journal of Alloys and Compounds*[J], 2014, 612: 56
28 Huang L J, Zhang Y Z, Geng L *et al. Materials Science and Engineering A*[J], 2013, 580: 242
29 Detrois M, Antonov S, Tin S *et al. Materials Characterization* [J], 2019, 157: 109 915
30 Song Z G, Xu C Z, Pu E X *et al*. *Rare Metal Materials and Engineering*[J], 2018, 47(3): 895
31 Gao S, Liu Z Q, Li C F *et al. Acta Materialia*[J], 2016, 110: 268
32 Wang L X, Jiang X, Dai F M *et al. Hot Working Technology*[J], 2016, 45: 153

粉末冶金高钨合金钢热变形行为与加工图

刘安晋[1,2]，王　琳[1,2]，程兴旺[1,2]，熊志平[1,2]，宁子轩[1,2]
(1. 北京理工大学 材料学院，北京 100081)
(2. 北京理工大学 冲击环境材料技术国家级重点实验室，北京 100081)

摘　要：在温度为900~1100 ℃、应变速率为0.001~1 s^{-1}的变形条件下，利用Gleeble热模拟试验机研究了粉末冶金工艺制备的新型高钨合金钢的热变形行为。结果表明：高钨合金钢的流变应力随应变率的降低和变形温度的升高而降低。构建高钨合金钢的Arrhenius双曲正弦函数本构方程及热加工图，得到高温变形激活能为377 kJ/mol，最佳变形工艺参数区间为1000~1100 ℃/0.001~0.01 s^{-1}。高温变形过程中，试样中有富钨μ相析出，在变形鼓胀区有微孔洞与微裂纹产生，数量随变形应变率的升高和温度的降低而增加，裂纹沿析出相萌生并扩展。同时μ相的析出提高了合金钢的高温强度。

关键词：高钨合金钢；热变形；本构方程；热加工图；微观组织

作者简介：刘安晋，男，1991年生，博士生，北京理工大学材料学院，北京 100081，E-mail：3120170528@bit.edu.cn